

Evaluation of pinhole collimator materials for micron-resolution ex vivo SPECT

Nguyen, Minh Phuong; Goorden, Marlies C.; Kamphuis, Chris; Beekman, Freek J.

DOI

[10.1088/1361-6560/ab1618](https://doi.org/10.1088/1361-6560/ab1618)

Publication date

2019

Document Version

Final published version

Published in

Physics in Medicine and Biology

Citation (APA)

Nguyen, M. P., Goorden, M. C., Kamphuis, C., & Beekman, F. J. (2019). Evaluation of pinhole collimator materials for micron-resolution ex vivo SPECT. *Physics in Medicine and Biology*, 64(10), Article 105017. <https://doi.org/10.1088/1361-6560/ab1618>

Important note

To cite this publication, please use the final published version (if applicable). Please check the document version above.

Copyright

Other than for strictly personal use, it is not permitted to download, forward or distribute the text or part of it, without the consent of the author(s) and/or copyright holder(s), unless the work is under an open content license such as Creative Commons.

Takedown policy

Please contact us and provide details if you believe this document breaches copyrights. We will remove access to the work immediately and investigate your claim.

Green Open Access added to TU Delft Institutional Repository

'You share, we take care!' – Taverne project

<https://www.openaccess.nl/en/you-share-we-take-care>

Otherwise as indicated in the copyright section: the publisher is the copyright holder of this work and the author uses the Dutch legislation to make this work public.

PAPER

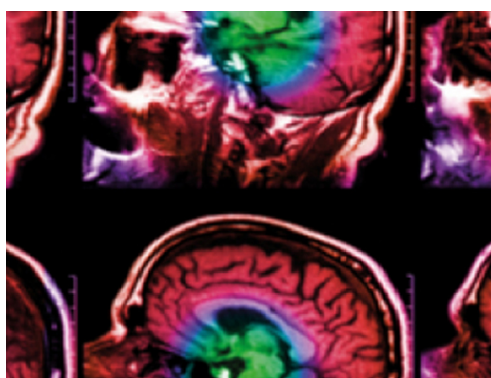
Evaluation of pinhole collimator materials for micron-resolution *ex vivo* SPECT

To cite this article: Minh Phuong Nguyen *et al* 2019 *Phys. Med. Biol.* **64** 105017

View the [article online](#) for updates and enhancements.

Recent citations

- [EXIRAD-3D: Fast automated three-dimensional autoradiography](#)
MinhPhuong Nguyen *et al*
- [Accelerated image reconstruction by a combined dual-matrix dual-voxel approach](#)
Marlies C Goorden *et al*



IPEM | IOP

Series in Physics and Engineering in Medicine and Biology

Your publishing choice in medical physics,
biomedical engineering and related subjects.

Start exploring the collection—download the
first chapter of every title for free.



PAPER

Evaluation of pinhole collimator materials for micron-resolution *ex vivo* SPECTRECEIVED
16 November 2018REVISED
1 April 2019ACCEPTED FOR PUBLICATION
4 April 2019PUBLISHED
16 May 2019Minh Phuong Nguyen^{1,4}, Marlies C Goorden¹, Chris Kamphuis² and Freek J Beekman^{1,2,3}¹ Section Biomedical Imaging, Delft University of Technology, Delft, The Netherlands² MILabs B.V., Utrecht, The Netherlands³ Department of Translational Neuroscience, Brain Center Rudolf Magnus, University Medical Center, Utrecht, The Netherlands⁴ Author to whom any correspondence should be addressed.E-mail: m.p.nguyen@tudelft.nl**Keywords:** collimator material, autoradiography, micron-resolution, Monte Carlo simulation, pinhole SPECTSupplementary material for this article is available [online](#)**Abstract**

Pinhole collimation is widely recognized for offering superior resolution-sensitivity trade-off in SPECT imaging of small subjects. The newly developed EXIRAD-3D autoradiography technique (MILabs B.V.) based on a highly focusing multi-pinhole collimator achieves micron-resolution SPECT for cryo-cooled tissue samples. For such high resolutions, the choice of pinhole material may have a significant impact on images. Therefore, this paper aims to compare the performance of EXIRAD-3D with lead, tungsten, gold, and depleted uranium pinhole collimators designed such that they achieve equal sensitivities. Performance in terms of resolution is characterized for several radioisotopes, namely ¹¹¹In (171 keV and 245 keV), ^{99m}Tc (140 keV), ²⁰¹Tl (71 keV), and ¹²⁵I (27 keV). Using Monte Carlo simulation, point spread functions were generated and their profiles as well as their full-width-at-half-maximum and full-width-at-tenth-maximum were determined and evaluated for different materials and isotopes. Additionally, simulated reconstructions of a Derenzo resolution phantom, validated with experimental data, were judged by assessment of the resolvable rods as well as a contrast-to-noise ratio (CNR) analysis. Our results indicate that using materials with higher photon-stopping power yields images with better CNR for the studied isotopes with improvements ranging from 1.9% to 36.6%. Visual assessment on the reconstructed images suggests that for EXIRAD-3D, the tungsten collimator is generally a good choice for a wide range of SPECT isotopes. For relatively high-energy isotopes such as ¹¹¹In, using gold inserts can be beneficial.

1. Introduction

The pinhole has enabled ultra-high-resolution 3D radionuclide imaging in small animals (Beekman and Van Der Have 2007). Since the use of pinholes in the earliest gamma cameras (Copeland and Benjamin 1949, Anger 1958, Mallard and Myers 1963), imaging systems with pinhole collimators have significantly evolved over the years pushing the imaging performance limits. A majority of preclinical SPECT systems is now equipped with multi-pinhole collimators leading to sub-millimetre resolution (Furenlid *et al* 2004, Beekman *et al* 2005, Metzler and Accorsi 2005, Kim *et al* 2006, Schramm *et al* 2006, Hesterman *et al* 2007, Meng *et al* 2009, Nuyts *et al* 2009, van der Have *et al* 2009, Golestani *et al* 2010, Sánchez *et al* 2013, Peterson *et al* 2015), even down to 0.25 mm (Ivashchenko *et al* 2014). Sub-millimetre resolution has also been achieved in imaging of PET isotopes and simultaneous imaging of PET and SPECT isotopes using clustered pinholes (Goorden *et al* 2013, Miwa *et al* 2015). Moreover, several multi-pinhole clinical SPECT systems are available on the market (Bocher *et al* 2010) or being developed (Bowen *et al* 2013, Lee *et al* 2014, Beekman *et al* 2015, King *et al* 2016, van Roosmalen *et al* 2016, Chen *et al* 2017, McDougal and Tornai 2017). Generally, the trade-off between resolution and sensitivity (i.e. the fraction of emitted gamma photons that are recorded by the detectors) of a pinhole collimator can be enhanced when the field-of-view is decreased. That is because the smaller the volume to be imaged, the closer the pinholes

can be placed to the radioactivity which increases sensitivity and leads to larger pinhole magnification factors which can enhance resolution.

On this line of development, MILabs B.V. has introduced EXIRAD-3D for SPECT scanning of cryo-cooled tissue samples, also called automated 3D autoradiography, which avoids time-consuming and error-prone steps present in traditional autoradiography. In traditional autoradiography, the tissue sample needs to be cryo-cooled, then sliced into thin sections, and scanned for hours or days with digital 2D films or phosphor screen readers. The obtained 2D images are subsequently registered to form a 3D volume representing the radioactivity distribution within the sample. This process potentially causes distortion in the 3D volume. With EXIRAD-3D, the whole tissue sample is cryo-cooled in a specially designed sample holder to avoid tracer leaking and tissue deformation, and scanned to form a 3D image. This novel technique is available on recent U-SPECT/CT and VECTor^{4,5&6}/CT systems, which are the successors of the systems described in van der Have *et al* (2009) and Goorden *et al* (2013). It uses a dedicated focusing multi-pinhole collimator made of tungsten alloy mounted within three large-field-of-view gamma-cameras with NaI(Tl) crystals in a stationary set-up. This collimator has a small bore size that allows high-resolution *ex vivo* scanning, but due to its small size, it is not suited for *in vivo* imaging. Due to the close pinhole-to-subject distance, EXIRAD-3D has a very high pinhole magnification and therefore can produce better than 140 μm spatial resolution (or 2.7 nl) ^{99m}Tc-SPECT images, which gets into the resolution range of traditional autoradiography (from 0.01 pl to several nl, Hargreaves *et al* 2015). Optimising the collimator could further improve the resolution-sensitivity trade-off for such systems.

Collimator and system geometry optimisation in general is complex as there is a high number of degrees of freedom, such as aperture diameter, pinhole placement, pinhole opening angle, pinhole orientation, number of pinholes, pinhole-detector distance, or pinhole material. Here we focus on the role of the material used. Aside from the commonly used lead and tungsten, gold and depleted uranium have been used for pinhole collimators (Jaszczak 1999, Tenney *et al* 2001, Beekman *et al* 2002, 2005, Peterson *et al* 2002, Tornai *et al* 2003, Furenlid *et al* 2004, van der Have *et al* 2009, Mejia *et al* 2010). Using materials with high stopping power is often preferred because it results in narrower point spread functions (PSFs) as photon penetration and scattering in the pinhole edges are reduced which can be expected to lead to better resolutions (van der Have and Beekman 2004). However, it would not be fair to judge the performance of pinhole materials only by their photon attenuation coefficient because the photons that are stopped by the material may contain information about their emission location that can still be useful in image reconstruction. One can instead compare resolution at equal sensitivities which can be accomplished by tuning the pinhole diameter for different materials. It was demonstrated in Bom *et al* (2011) that with equal sensitivities, the PSF full-width-at-half-maximum (FWHM) increased from lead, tungsten, gold, to uranium, while the PSF full-width-at-tenth-maximum (FWTM) decreased. However, the resolutions of final reconstructed images were almost independent of the material used for the SPECT systems investigated in that work. This implies that good system modelling for image reconstruction can at least partly compensate for pinhole edge penetration and scattering, and the evaluation of pinhole materials should be based on final reconstructed images. For a higher resolution system as EXIRAD-3D, it is not *a priori* clear if the findings from Bom *et al* (2011) still hold as the performance of such a system can be more sensitive to the collimator material used.

This paper aims to compare EXIRAD-3D pinhole collimators made of different materials at equal system sensitivities. Four collimator materials (lead, tungsten, gold, and depleted uranium) were investigated for several radioisotopes, namely ¹¹¹In (171 keV and 245 keV), ^{99m}Tc (140 keV), ²⁰¹Tl (71 keV), and ¹²⁵I (27 keV). For each isotope, Monte Carlo simulation (MCS) of a full multi-pinhole collimator was performed to tune the pinhole diameters such that all collimators investigated obtained equal sensitivity. We then compared PSFs and reconstructed Derenzo resolution phantom images for different materials and isotopes.

2. Methods

2.1. EXIRAD-3D system with multi-pinhole collimator

For EXIRAD-3D imaging, the U-SPECT/CT or VECTor/CT system is equipped with a focusing multi-pinhole collimator mounted within three large-field-of-view gamma-cameras having 3.5 mm intrinsic spatial resolution and 10% FWHM energy resolution at 140 keV. Each gamma-camera is equipped with a 9.5 mm thick NaI(Tl) crystal having a usable area of 497.4 * 410.6 mm² and read out by 55 photomultiplier tubes (PMTs). The collimator's core is cylindrical with an inner bore diameter of 10.5 mm and a wall thickness of 7.5 mm (figures 1(a) and (b)) made of a tungsten alloy containing 92.5% tungsten, 5.25% nickel, and 2.25% iron. It has a total of 87 round knife-edge pinholes with pinhole centres at a radius of 12.5 mm from the z-axis (see figure 1 for axes definition). The pinhole axes converge at a single point at the collimator centre, and they are distributed into five rings with the tilt angles indicated in figure 1(a). There is also an 8° angular shift around the z-axis between adjacent rings. All pinholes have the same aperture diameter of 0.15 mm, and an opening angle of 26°. The core

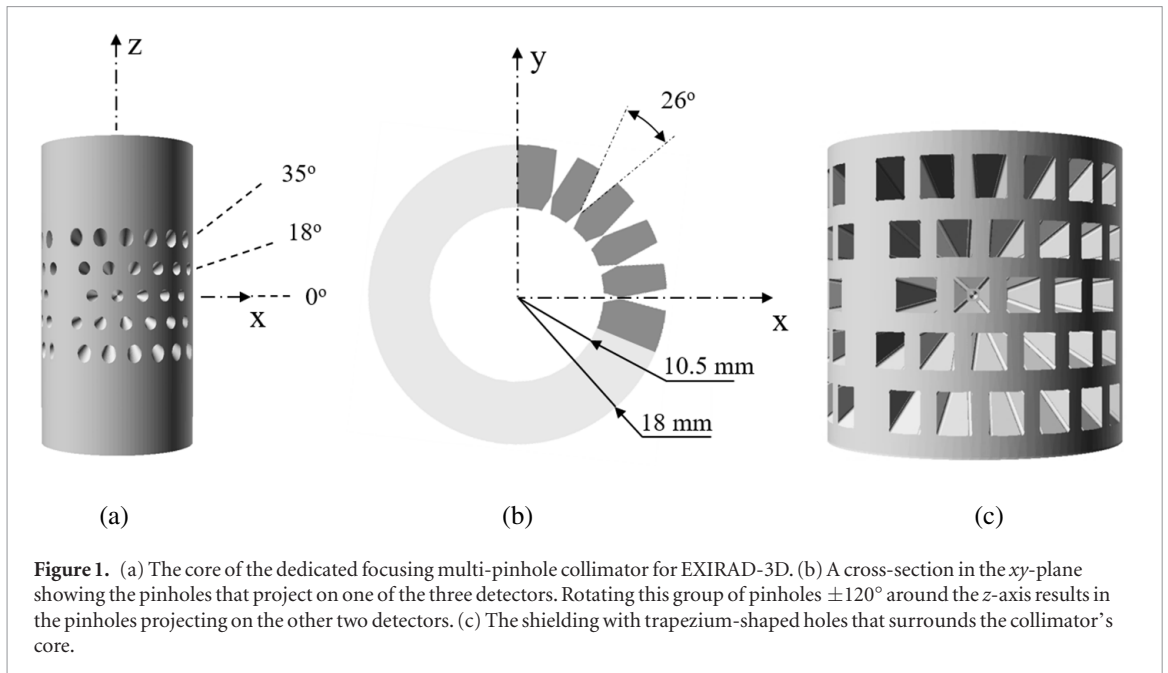


Figure 1. (a) The core of the dedicated focusing multi-pinhole collimator for EXIRAD-3D. (b) A cross-section in the xy -plane showing the pinholes that project on one of the three detectors. Rotating this group of pinholes $\pm 120^\circ$ around the z -axis results in the pinholes projecting on the other two detectors. (c) The shielding with trapezium-shaped holes that surrounds the collimator's core.

is surrounded by an lead shielding tube with trapezium-shaped holes to prevent overlapping between pinhole projections (figure 1(c)).

2.2. Monte Carlo simulations

To simulate photon transport in the collimator and detector, we used the well-validated Monte Carlo simulation (MCS) software Geant4 Application for Tomographic Emission (GATE) (Jan *et al* 2004, 2011, Staelens *et al* 2006, Chen *et al* 2008). GATE version 8.0 was used with Geant4 version 10 on a CentOS 6.6 cluster with 250 processors running simultaneously. Modelled physics processes include photoelectric effect, Compton scattering, and Rayleigh scattering for gamma photons, as well as ionisation, bremsstrahlung, and multiple scatter for electrons. To simulate the triangular detector geometry, a set of three NaI-scintillators was created natively in GATE using three $497.4 \times 410.6 \times 9.5 \text{ mm}^3$ rectangular boxes. The first scintillator was placed perpendicularly to the y -axis and centred at $(0 \text{ mm}, -210 \text{ mm}, 0 \text{ mm})$, and the other two were created by rotating the first one by $\pm 120^\circ$ around the z -axis. Other details of the detectors such as exact light guide geometry and PMTs were not explicitly simulated in GATE but captured in the detector resolution (explained in equation (1)). The collimator was mostly based on a computer-aided design (CAD) of the real commercialised collimator to keep precise pinholes and shielding's geometries, while we adjusted pinhole diameter and collimator material for this study. Since the role of material is most important on the pinhole edges and a lead shielding would perform as well as a shielding made of tungsten, gold, or uranium, we assumed that the whole collimator contains a single material without assigning a different material (lead) to the shielding. An STL file of the collimator exported from the CAD program was inserted into GATE. This STL file format is only supported in GATE for version 8.0 and higher. We made sure the STL meshes well resembled the continuous model by using a large number of triangles, especially at the pinhole apertures. On average, each collimator is composed of 170 900 triangular faces, and each pinhole aperture is formed by 40 aperture blades. A reasonable 12 min time was required to render an STL collimator. The STL files were prepared in Netfabb (Autodesk, Inc., San Rafael, California) to remove unexpected gaps, non-manifold edges/vertices, and intersecting triangles before importing it into GATE. GATE outputs the interaction time, total deposited energy, and energy-weighted average interaction location in the scintillators for each gamma photon. Photon interaction locations were sampled with a pixel grid of $1.072 \times 1.072 \text{ mm}^2$ (pixel size of the experimentally used detector). A digital detector mask was applied to mask areas where no direct photons from the object are expected to be detected as is also done in the reconstruction software of the real system (van der Have *et al* 2008).

The full isotopes' emission spectrum and activity decay, retrieved from Chu *et al* (1998), were considered for each studied isotope. In addition, we randomised the interaction energy and position for each event using Gaussian probability distributions to simulate the detector's energy resolution and spatial resolution. Energy dependence of these resolutions was taken into account as summarised in table 1. As these resolutions were only determined experimentally for a few energy values (indicated in bold in the table), the rest of them was calculated using models from literature. For the detector's energy resolution we used (Jan *et al* 2004):

$$R_{\text{energy}} = \sqrt{2.35^2 \frac{1.1}{LEp\bar{e}} + R_i^2}, \quad (1)$$

Table 1. MCS settings for different isotopes. For spatial resolution and energy resolution of the detector, numbers in bold denote experimentally determined values, and the rest is calculated using equations (1) and (2).

Isotope	Peak energies (keV)	Half-life	Detector's spatial resolution (mm)	Detector's energy resolution (%)	Photopeak windows
¹¹¹ In	245	2.8 days	2.6	8.5	20% at 245 keV
	171		3.2	9.4	20% at 171 keV
^{99m} Tc	140	6.0 hours	3.5	10	20% at 140 keV
²⁰¹ Tl	71	3.0 days	4.9	12.7	40% at 71 keV
¹²⁵ I	27	59.4 days	8.0	25	60% at 27 keV

where L , E , \bar{p} , $\bar{\epsilon}$, and R_i are light yield, deposited energy, light collection efficiency (i.e. the fraction of scintillation photons that arrive at the PMTs' photocathodes), quantum efficiency of the PMTs, and intrinsic resolution of the detector in FWHM, respectively. Here we set for the NaI(Tl) detector a light yield of 38 photons keV⁻¹, a quantum efficiency of 30%, and 6% FWHM intrinsic energy resolution. These values were retrieved from Moszyński *et al* (2002), Hamamatsu (2007) and Saint-Gobain. Then, with the measured detector's energy resolution at 140 keV of 10% FWHM, the light collection efficiency was calculated to be 59.5%. The detector's spatial resolution was measured for our system to be 3.5 mm FWHM at 140 keV, and scaled by the reciprocal of the square root of the photon's energy, as was also done in other studies (Metzler and Accorsi 2005, Rong *et al* 2012):

$$R_{spatial} = 3.5\sqrt{140/E}, \quad (2)$$

where E is deposited energy in keV. Note that even though the detector's spatial resolution is in the mm range, system resolution can be significantly better due to the high pinhole magnification (Accorsi and Metzler 2004), and reconstructed resolution can be even better than the system resolution when accurate photon transport and detector blurring are modelled in image reconstruction. Table 1 also presents some of the isotopes' properties and the photopeak windows for acquisition. For ¹¹¹In, which has two prominent photopeaks, data from both photopeaks are acquired simultaneously.

2.3. Determination of pinhole diameters to obtain equal sensitivities

For each isotope, the pinhole aperture diameter was adjusted to obtain equal sensitivity for different materials. To this end, we simulated projections of a uniform activity distribution with the size of the central field-of-view (CFOV)—a cylinder with a diameter and a length of 4 mm that can be observed simultaneously by all pinholes—and sensitivity was calculated as the number of detected counts within the photopeak window over the simulated number of emissions ($5.5 * 10^9$). This way, we obtained the average sensitivity over the CFOV. For each isotope used, we always fixed the pinhole diameter for the tungsten collimator to 150 μm (diameter of the pinholes in the real collimator) and varied the pinhole diameter with a step size of 2 μm for other materials to achieve (nearly) equal sensitivity. Characteristics of the four investigated materials are provided in table 2 at the energies corresponding to the primary emission of the considered radioisotopes, namely ¹²⁵I, ²⁰¹Tl, ^{99m}Tc, and ¹¹¹In. Note that here we only simulated pure materials. In actual collimator manufacturing, alloys of these materials are often used. The influence of this is discussed further at the end of this paper.

2.4. PSF comparison for single pinholes

By comparing the PSFs obtained with different collimator materials at equal system sensitivities, we analysed the magnitude of the pinhole penetration and scatter components in the pinhole projections. To this end we considered the PSF projecting from a point source at the collimator's centre through a pinhole oriented perpendicular to one of the detector planes. The number of emitted gamma rays was set to $4 * 10^{11}$. Only for this comparison, the PSFs were sampled to a smaller grid of $0.2 * 0.2$ mm² on the gamma detector, instead of the customarily used pixel size of $1.072 * 1.072$ mm² when we make projections. We compared the 2D PSFs and their profiles, as well as FWHMs and FWTMs. To calculate a PSF's FWHM (or FWTM), we fit the PSF to a 2D Gaussian shape using the Levenberg–Marquardt algorithm (Levenberg 1944, Marquardt 1963), and drew a contour on the fitted PSF that represents the isoline at the intensity equal to one half (or one-tenth) of its maximum using the marching squares algorithm (Maple 2003). Then, the average diameter of the contour was taken and projected back to the image domain by dividing it by the pinhole magnification factor to obtain the FWHM (or FWTM).

2.5. Multi-pinhole reconstruction

2.5.1. Phantom scan simulation

A Derenzo phantom having six sectors of hollow cylindrical rods with varying diameters that contained a radioactive solution inside was simulated (figure 2). In each sector, the distance between centres of two adjacent rods was twice the rod diameter. The phantom was created natively in GATE, so it had no discretisation.

Table 2. Densities and attenuation coefficients of the studied materials at the considered energies. The values were obtained from NIST (Seltzer 1993, Hubbell and Seltzer 1995).

Materials	Density (g cm ⁻³)	Linear attenuation coefficient μ (mm ⁻¹)				
		27 keV (¹²⁵ I)	71 keV (²⁰¹ Tl)	140 keV (^{99m} Tc)	171 keV (¹¹¹ In)	245 keV (¹¹¹ In)
U	18.95	102.567	8.754	5.800	3.604	1.550
Au	19.32	69.730	5.688	4.260	2.560	1.114
W	19.30	57.577	20.482	3.621	2.200	0.952
Pb	11.53	45.077	3.703	2.751	1.655	0.708

For each radioisotope, a realistic activity concentration that can be attained in animal experiments was simulated on the phantom: 26.3 MBq ml⁻¹, 212 MBq ml⁻¹, 8.8 MBq ml⁻¹, and 185 MBq ml⁻¹ for ¹¹¹In, ^{99m}Tc, ²⁰¹Tl, and ¹²⁵I, respectively. The activity concentrations for ^{99m}Tc and ¹²⁵I were derived from real experimental scans of a mouse knee joint and a mouse thyroid on our EXIRAD-3D system. In the knee joint scan, 300 MBq ^{99m}Tc-methylene diphosphonate was injected into a mouse and bone tissue containing 6 MBq activity was imaged. In the thyroid scan, 39 MBq ¹²⁵I-Na was injected into a mouse and thyroid tissue containing 1.6 MBq activity was imaged. The activities on the tissues were measured in a dose calibrator (VDC-304, Veenstra Instruments, the Netherlands). Knowing the total activity in the tissue sample and the activity distribution on the corresponding SPECT image, the activity concentration (MBq ml⁻¹) for each image voxel was calculated. Then, the average activity concentration over the knee joint or the thyroid was used for simulations in this paper. Note that in this study the animal was sacrificed and its tissue was cryo-cooled shortly after activity injection. In this case, radiation-induced biological effects do not play a role. The activity concentrations for the other isotopes were obtained from biodistribution studies from literature (Hijnen *et al* 2011, Willekens *et al* 2016) which were for *in vivo* scans.

A total scan time of 16 h was simulated assuming an overnight scan, and activity decay was taken into account for each isotope. The scanning focus method (Vastenhouw and Beekman 2007) in which the phantom is scanned at multiple bed positions and images are reconstructed from all projection data of the different bed positions was used to improve sampling. A total of nine bed-positions on a plane perpendicular to the collimator axis were simulated in GATE with equal scan time for each position.

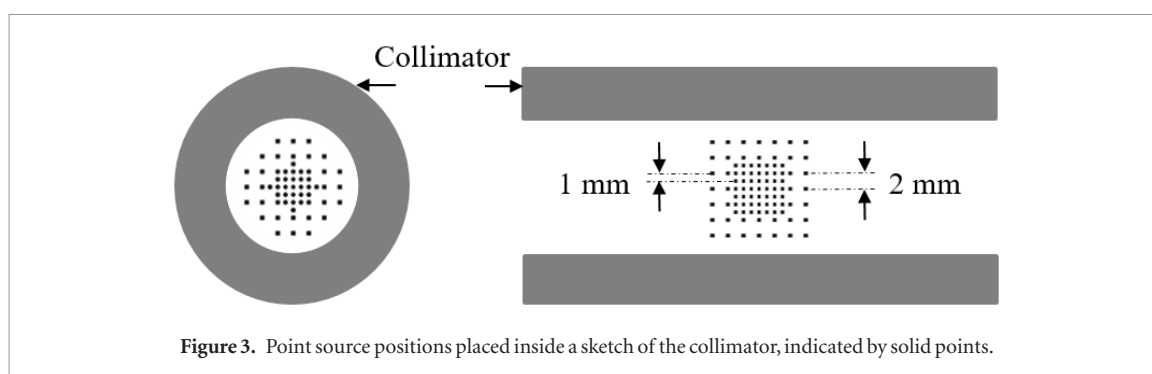
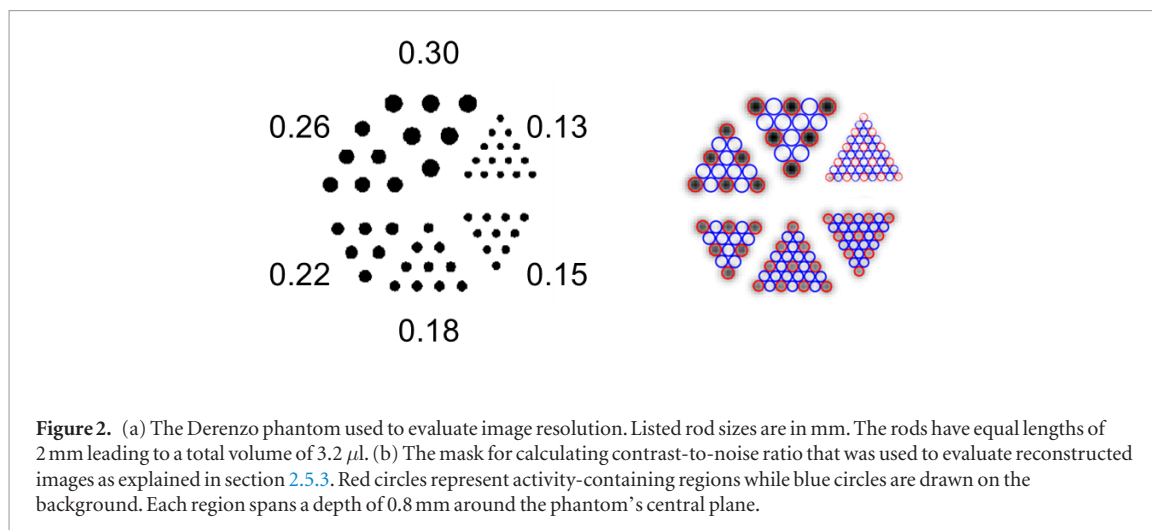
We also simulated realistic background radiations that could be significant in these phantom scans as the activity contained in the small-volume phantom (3.2 μ l) was rather low. To this end, the count rate from the background radiation within the photopeak window for each isotope in table 1 was measured with a U-SPECT/CT system at MILabs B.V., Utrecht, the Netherlands to be 175 cps, 60 cps, 100 cps, and 45 cps for ¹¹¹In (both photopeak windows), ^{99m}Tc, ²⁰¹Tl, and ¹²⁵I, respectively. Then with the assumption that the background counts are uniformly distributed over the detector pixels, the average number of background counts on each detector pixel over the scan time per bed position was calculated, and its Poisson realisation was added to the projection at that pixel.

For each simulated scan, the photons that deposit energy in the two side windows adjacent to the photopeak, each having a width of 25% of the photopeak window's width, were also recorded for the purpose of scatter correction. Background counts were also added to the side window projections in the same way as for the photopeak window. Here, the number of counts from background radiation within a side window was assumed to be 25% of the number of counts from background radiation within the corresponding photopeak window.

2.5.2. System matrix generation

Accurate modelling of the system matrix is necessary for high-quality reconstructed images. The matrix, consisting of PSFs corresponding to all voxels in the field of view, represents the probabilities that a photon emitted from a voxel is recorded at a detector pixel. In this study, we based the matrix generation method on the one that is experimentally used and described in van der Have *et al* (2008). In this method, a limited number of PSFs is measured, and then a full matrix is obtained by model-based interpolation. This approach currently performs well in reconstructing the EXIRAD-3D experimental scan data (Nguyen *et al* 2017). We used the MCS described in section 2.2 to simulate the point source measurements mimicking what is done in the experimental procedure.

For each matrix generation, a total of 435 point source positions was simulated with GATE. They were placed on a 1 mm grid near the collimator's centre and a 2 mm grid further away from the centre (figure 3). We assumed that for ^{99m}Tc the point source contained an activity of 46 MBq and was scanned for 15 s at each position, as in the common experimental procedure. For the other isotopes, the same number of emitted photons was assumed from the point source. This way the simulation took 3 d.



The number of point source positions is just $1/200\,000$ of the required number of image voxels in the system matrix for a 0.05 mm voxel size. The model-based interpolation procedure is based on transforming a nearby PSF using some estimated parameters (PSF's flux, width, and centre location) and is explained in detail in van der Have *et al* (2008). For multi-pinhole collimation, it is not necessary to store all voxel-pixel combinations in the system matrix because only the photons that go through the pinholes or pass the pinhole's edge have considerable probabilities to be detected. Therefore, the PSF parts having negligible intensities are not saved such that $C\%$ of the area under the PSF is excluded. $C\%$ was set to 4%, except for ^{125}I ($C\% = 10\%$) to keep reasonable matrix sizes on disk. Reducing the matrix size also helps to speed up image reconstruction.

The shielding with trapezium-shaped holes surrounding the collimator makes sure that each pinhole projects in a separate segment on the gamma camera and a precise segmentation of the detector area into these separate segments needs to be known for an accurate system matrix (van der Have *et al* 2008). To obtain this, we simulated a high-count projection of a uniformly filled cylindrical activity volume (radius 10 mm, length 16 mm) that just fits inside the collimator and was assumed to emit 10^{11} gamma photons. This number of photons was not as high as in the real experiment to avoid long computation times, but it was sufficient to derive a proper segmentation. This step was done only once for all simulated collimators because the pinhole position and shielding tube did not change.

2.5.3. Image reconstruction and evaluation

Reconstructions were performed using the similarity-regulated ordered-subset expectation maximisation (SROSEM) algorithm (Vaissier *et al* 2016). The maximum number of subsets was set to 128, and all images were reconstructed on an isotropic 0.05 mm-voxel grid. Scatter and background radiation were corrected using the triple-energy window method (Ogawa *et al* 1991). The reconstructed images were post-filtered using a 3D Gaussian filter with FWHM in the range of 0.06–0.30 mm with a step size of 0.01 mm. The optimal number of iterations and filter size were defined to be those that maximised the average contrast-to-noise ratio (CNR, calculation explained below). The image reconstruction was validated by comparing an experimental result with a simulation result of the same scan which was a resolution phantom scan with $800 \text{ MBq ml}^{-1} \text{ } ^{99\text{m}}\text{Tc}$ using the tungsten collimator. The evaluation of collimator materials was based on the CNRs as well as visual assessment over the reconstructed rod shapes and minimally resolvable rod sizes on the Derenzo phantom.

CNR was calculated in the same way as in Walker *et al* (2014). To this end, regions of interest (ROIs) were used as shown in figure 2(b). Red circles indicate the regions with activity and blue circles indicate the background

Table 3. The pinhole diameters for different materials that were adjusted to achieve equal sensitivity over the CFOV for each radioisotope. The corresponding system sensitivities are also listed.

Isotopes	System sensitivity over the CFOV (%)	$d_{\text{ph-U}}$ (mm)	$d_{\text{ph-Au}}$ (mm)	$d_{\text{ph-W}}$ (mm) (fixed)	$d_{\text{ph-Pb}}$ (mm)
^{111}In	0.108	0.232	0.184	0.150	0.054
$^{99\text{m}}\text{Tc}$	0.090	0.174	0.160	0.150	0.126
^{201}Tl	0.044	0.144	0.130	0.150	0.102
^{125}I	0.050	0.154	0.152	0.150	0.148

regions. Each region spans a depth of 0.8 mm (16 slices) around the phantom's centre. We defined the contrast of each of the six rod-sectors as:

$$C_s = \frac{\bar{I}_s - \bar{B}_s}{\bar{I}_s}, \quad (3)$$

where \bar{I}_s is the mean intensity over the activity regions of sector $s(I_s)$ and \bar{B}_s is the mean intensity over the background regions of sector $s(B_s)$. CNR of each sector was defined as C_s/N_s where:

$$N_s = \frac{\sqrt{\sigma_{I_s,p}^2 + \sigma_{B_s,p}^2}}{\bar{I}_s}, \quad (4)$$

serving as a measure of variability between ROIs. There, $\sigma_{I_s,p}$ and $\sigma_{B_s,p}$ are standard deviations over I_s and B_s , respectively, calculated over all sectors s and a subset of planes p , given by $\{1, 4, 7, 10, 13, 16\}$ to reduce inter-ROI covariance, and \bar{I}_s is mean intensity over all ROIs in sector s . Then the average of the CNRs over the sectors with visible rods was taken for the image quality assessment.

3. Results

3.1. Pinhole diameters to obtain equal sensitivities for different collimator materials

In table 3, pinhole diameters that result in an almost equal sensitivity over the CFOV for different materials and different isotopes are provided. For all cases, the remaining sensitivity differences due to the fact that pinhole diameter was changed in discrete 2 μm steps were small, less than $10^{-4}\%$. As expected, table 3 indicates that to obtain 'equal' sensitivities, when using a material with higher photon-absorption power larger pinholes are required. Note that 71 keV (^{201}Tl) is close to the K-edge of tungsten where its attenuation coefficient increases suddenly; therefore, it is reasonable that for ^{201}Tl the tungsten pinholes have larger aperture diameter than the pinholes made of other materials.

3.2. PSF comparison

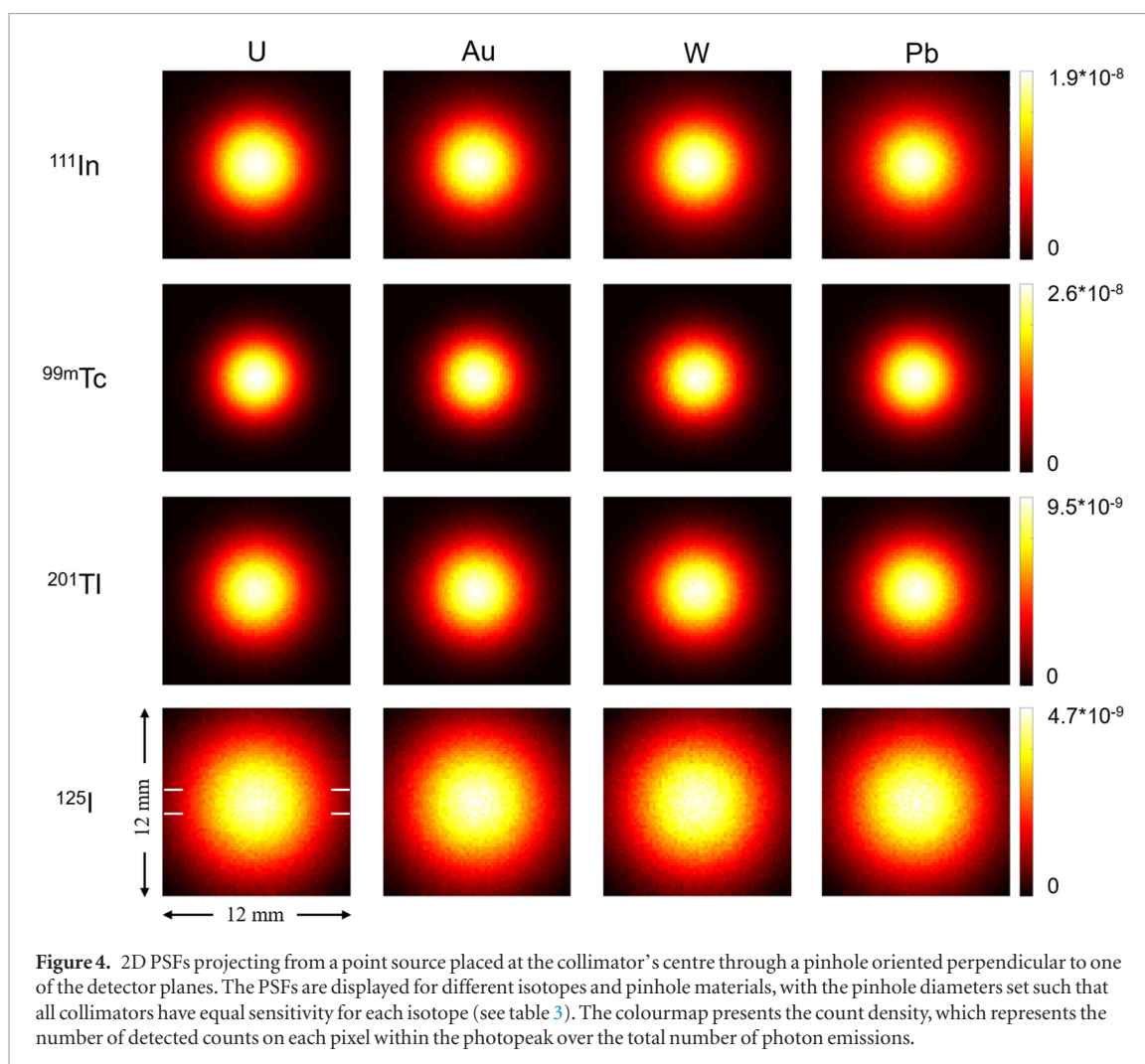
The 2D PSFs through a pinhole projecting perpendicular to the detector with diameter as summarised in table 3 are shown in figure 4 while profiles are provided in figure 5. For ^{111}In , a difference between PSFs for the various collimator materials is visually distinguishable: the PSF is slightly wider when using a material with lower attenuation coefficient. This visual distinction is hard to make for other isotopes having lower energy than ^{111}In .

Given that the number of photons emitted from the point source is always fixed to be $4 * 10^{11}$, the unequal maximal values of the PSFs between different isotopes as indicated in the color bar in figure 4 are due to the fact that the percentage of emitted photons that ends up depositing energy within the photopeak window depends on the energy distribution of the isotope's emission spectrum. These numbers are also affected by the level of detector's spatial blurring, which is energy dependent.

The PSFs' profiles in figure 5 are plotted as a function of the distance from the PSF centre on a semi-logscale, and the corresponding FWHM and FWTM are presented in figure 6. Almost identical profiles and FWHM/FWTM are observed for the different pinhole materials for the low-energy ^{125}I . A distinction between materials is observable for ^{201}Tl and $^{99\text{m}}\text{Tc}$ and more prominent for ^{111}In . Generally, under the condition of equal sensitivity, the use of materials with higher stopping power yields PSFs with narrower tail and lower values for the FWHM and FWTM.

3.3. Multi-pinhole reconstruction

A validation of the simulations performed in this paper is provided in figure 7. Here tungsten pinholes with an aperture diameter of 0.15 mm were assumed, and the resolution phantom was filled with $^{99\text{m}}\text{Tc}$. With an activity concentration of 800 MBq ml $^{-1}$, the minimally visible rods on the phantom have a diameter of 0.15 mm, which is in agreement with the experiment in which the phantom was filled with the same amount of activity and scanned in the real tungsten-alloy collimator. Note that the phantom used in the experiment has slightly different



rod sectors from the one used in the simulation because it is of interest to check in the simulation the 0.13 mm rods that were not included in the experimental phantom. Figure 7 also provides an impression of the achievable resolution with EXIRAD-3D for ^{99m}Tc for various activity concentrations.

Figures 8–11 show images of the resolution phantom for realistic biological activity concentrations for ^{111}In , ^{99m}Tc , ^{201}Tl , and ^{125}I , respectively. Images are displayed at several iterations, and the square boxes indicate the images with the highest average CNR averaged over the visible rods. Note that the range of the optimal number of iterations varies across isotopes used (across figures 8–11) and thus different iteration number ranges are shown for different isotopes. The smallest rods that can be resolved have a size of 0.15 mm for ^{99m}Tc , 0.22 mm for ^{111}In and ^{125}I , and 0.26 mm for ^{201}Tl . Visual assessment indicates that uranium and gold perform slightly better than tungsten and lead by offering clearer images, specially for ^{111}In (see the phantom's background in figure 8). For ^{125}I , all simulated images appear visually similar, independent of material used.

Figure 12 summarises all the optimal average CNRs in figures 8–11 along with CNR for each visible rod sector. Generally, the CNR is increasing when using a higher-stopping-power material. Compared to lead, the use of materials with higher attenuation coefficient improves the average CNR up to 36.6%, 4.6%, 7.2%, and 1.9% for ^{111}In , ^{99m}Tc , ^{201}Tl , and ^{125}I , respectively.

4. Discussion

We have compared the performance of EXIRAD-3D with various pinhole materials regarding resolution at equal system sensitivities. Four pinhole materials, namely lead, tungsten, gold, and depleted uranium, have been investigated for a wide range of photon energies (27 keV–245 keV). The results show that the pinhole material has an influence on the image resolution when the pinhole diameter is adjusted to keep sensitivity unchanged. Using a material with higher photon stopping power improves image quality, especially for high photon energies. The pinhole material matters for this high-resolution system because with the small pinholes used, the proportion of the number of penetrative and scattered photons compared to the number of photons passing directly through the pinhole can be significant and the material's ability to attenuate photons becomes important. This

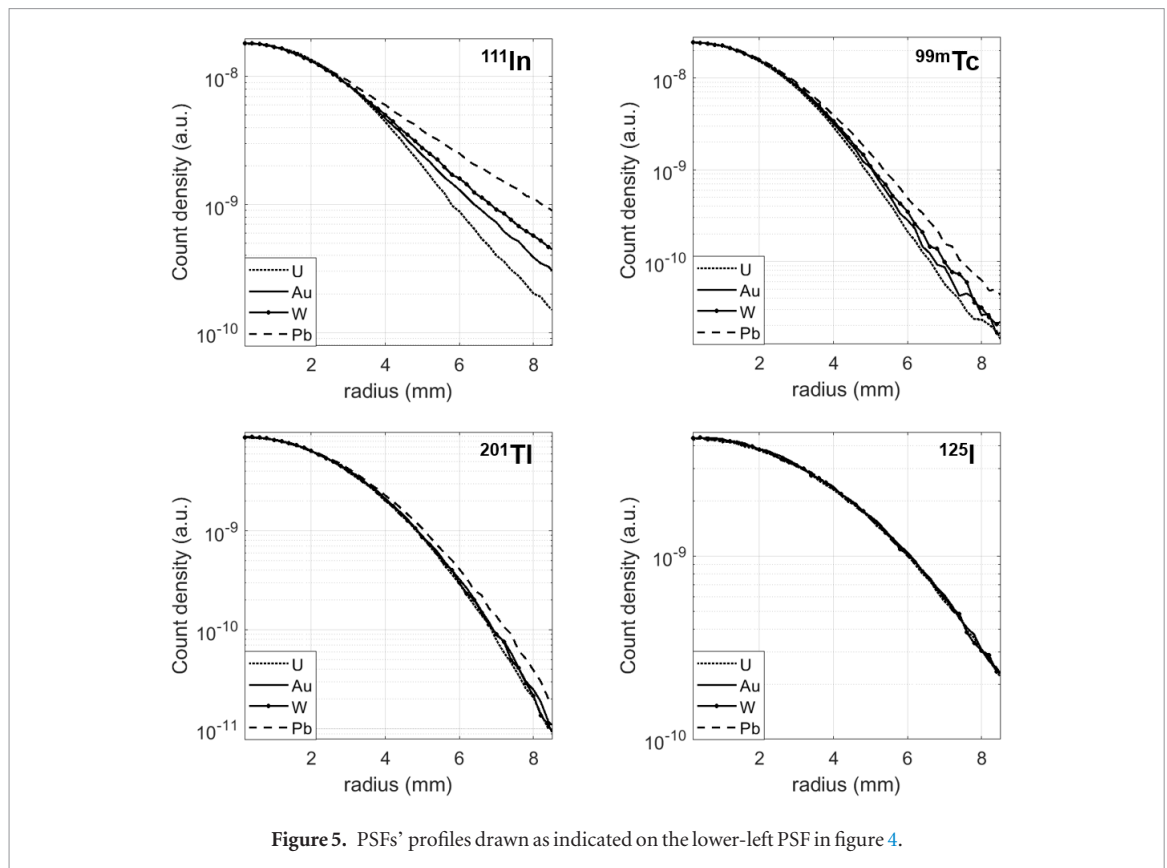


Figure 5. PSFs' profiles drawn as indicated on the lower-left PSF in figure 4.

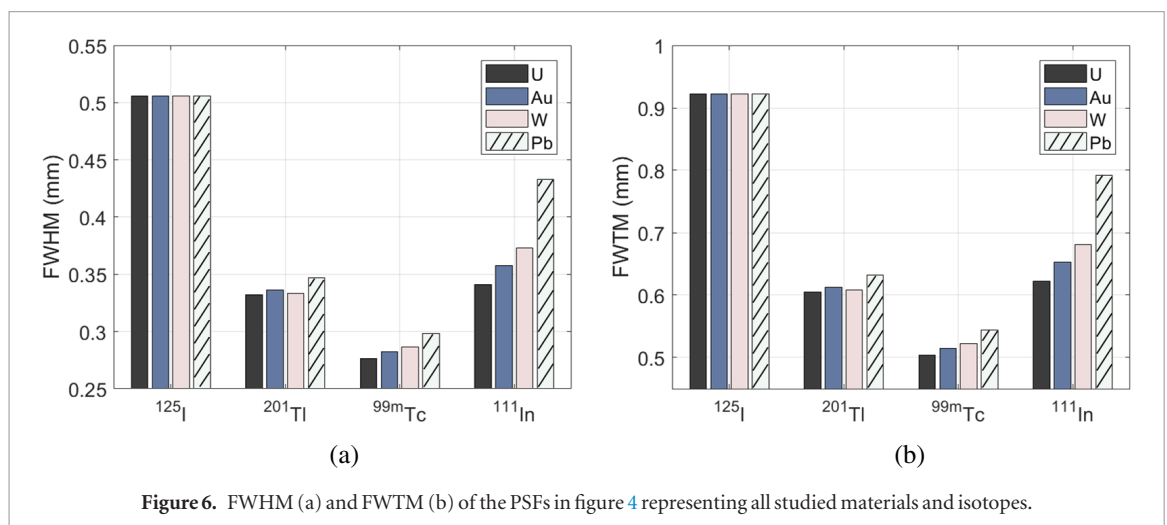
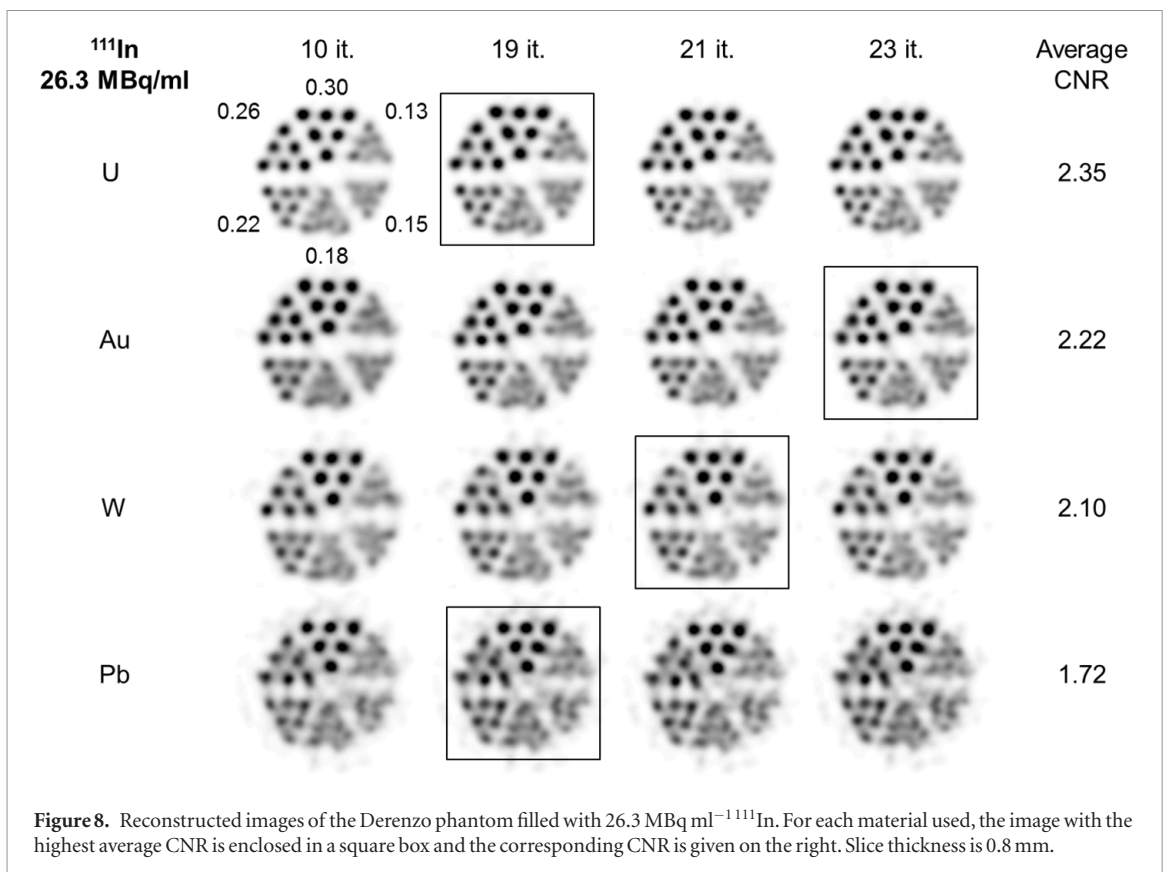
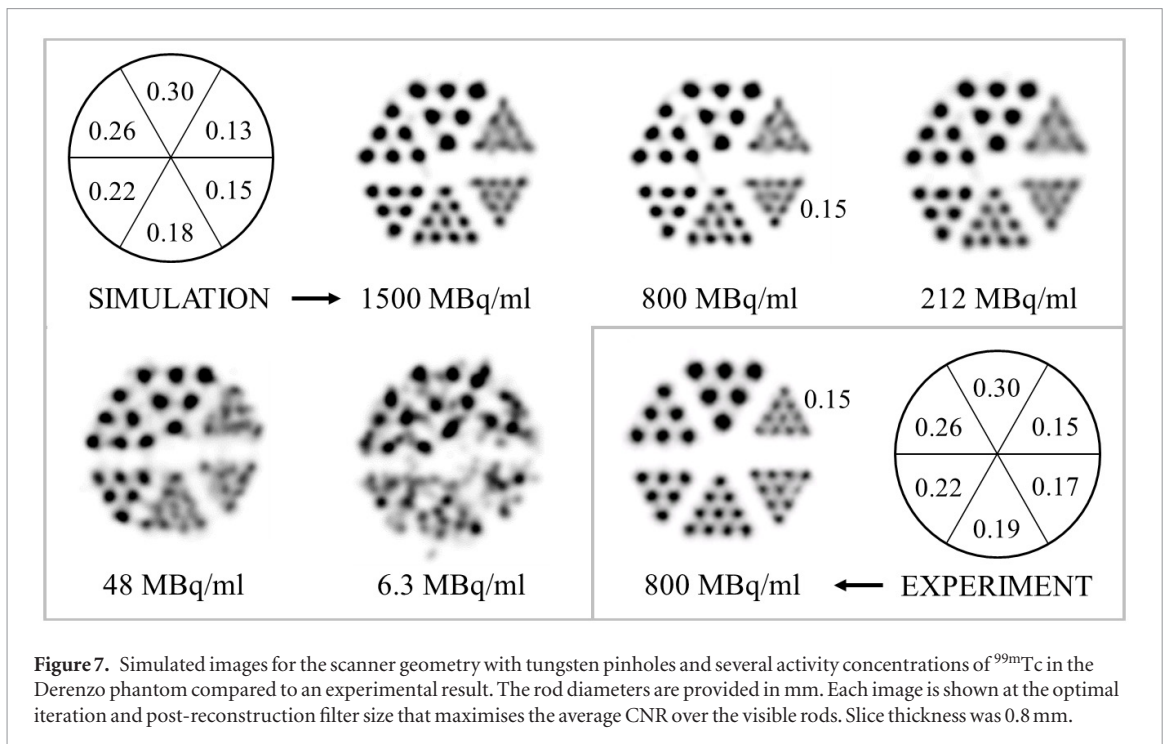


Figure 6. FWHM (a) and FWTM (b) of the PSFs in figure 4 representing all studied materials and isotopes.

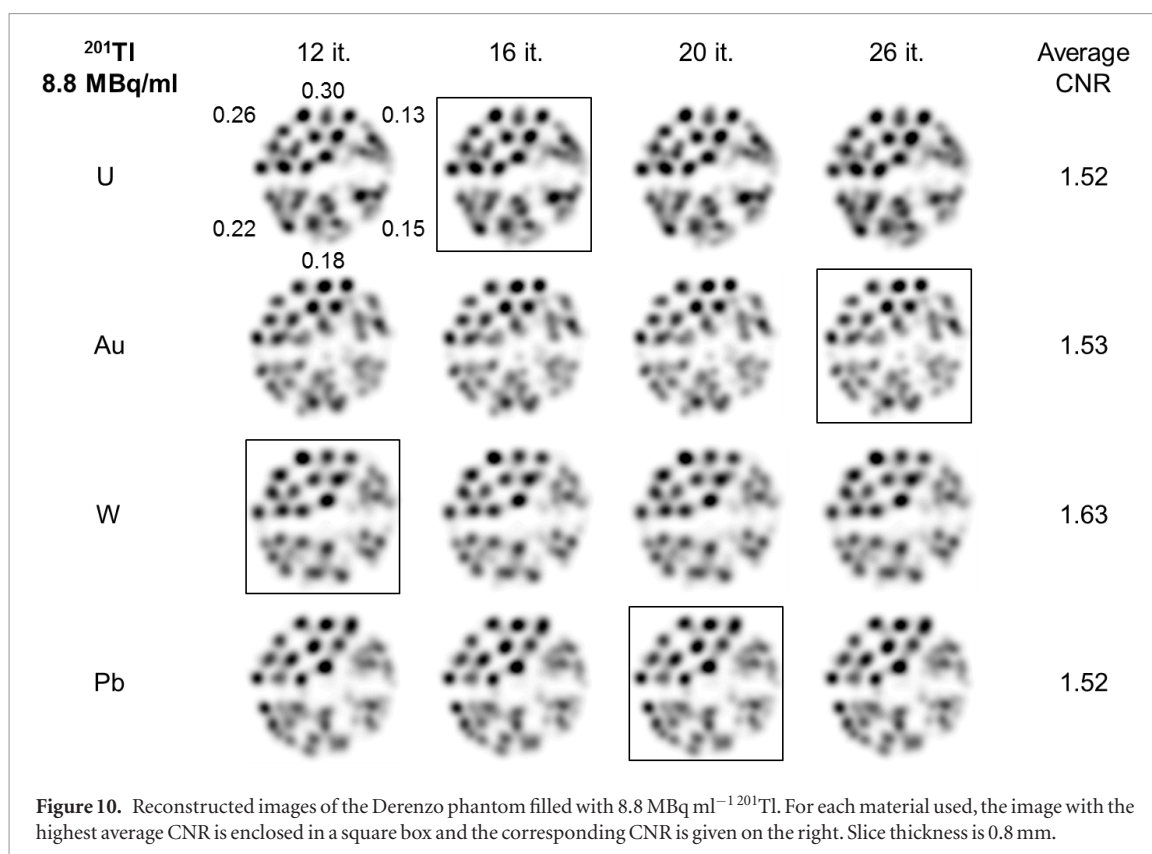
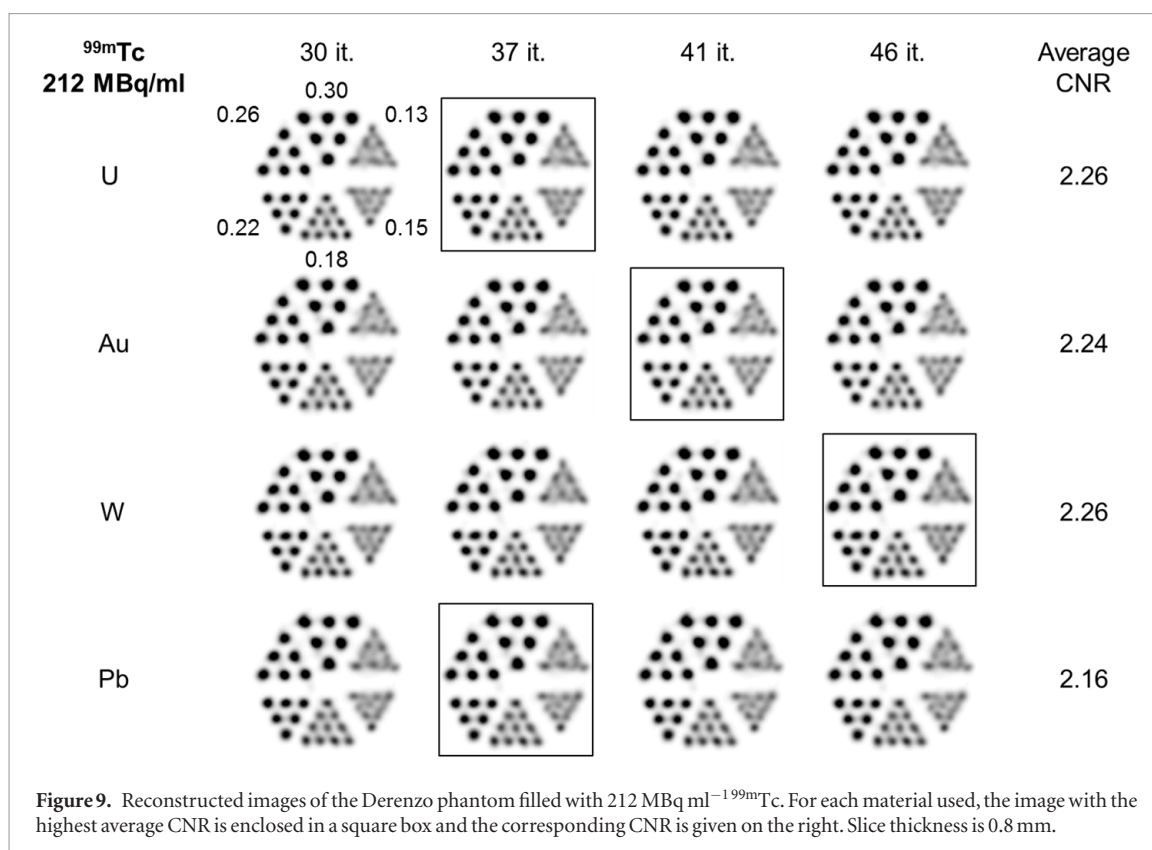
proportion reduces with the higher-stopping-power material, and thus image quality can be improved. Besides, the chosen pinhole material matters more for the higher energy isotopes as in that case the relative contribution of the pinhole to the PSF is larger; with an average pinhole magnification factor of 19 which we calculated for this geometry (taking into account that the pinholes project onto flat detectors), the detector's contribution to the resolution is about 2.7, 1.6, 1.2, and 0.97 times that of the pinhole for ^{125}I , ^{201}Tl , $^{99\text{m}}\text{Tc}$, and ^{111}In , respectively.

We performed a validation by simulating a scan with $800 \text{ MBq ml}^{-1} \text{ }^{99\text{m}}\text{Tc}$ that mimics an experimental scan and achieved comparable images. When assessing images obtained with different pinhole materials, biological activities were assumed because it is of interest to investigate the resolution achievable in realistic animal scans. Therefore, ^{111}In , $^{99\text{m}}\text{Tc}$, ^{201}Tl , and ^{125}I with activity concentrations of 26.3 MBq ml^{-1} , 212 MBq ml^{-1} , 8.8 MBq ml^{-1} , and 185 MBq ml^{-1} , respectively, were put in the resolution phantom. With these activities, the smallest rods that the system could resolve have diameters of 0.15 mm for $^{99\text{m}}\text{Tc}$, 0.22 mm for ^{111}In and ^{125}I , and 0.26 mm for ^{201}Tl . Compared to $^{99\text{m}}\text{Tc}$, high-energy ^{111}In results in more undesirable penetration and scatter in the pinhole edges, while low-energy ^{125}I has the disadvantage of worse detector's spatial and energy resolutions. The resolution obtained with ^{201}Tl is also degraded as its activity on the phantom was rather low. The achievable image resolutions could be improved when scan time is increased by, for example, scanning over the weekend, which is



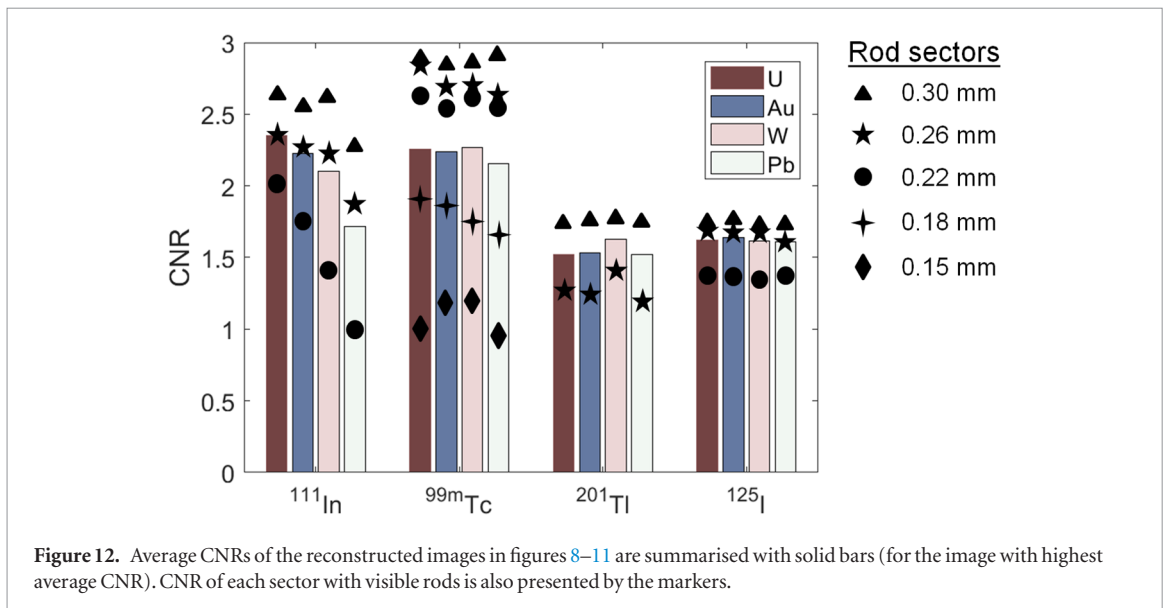
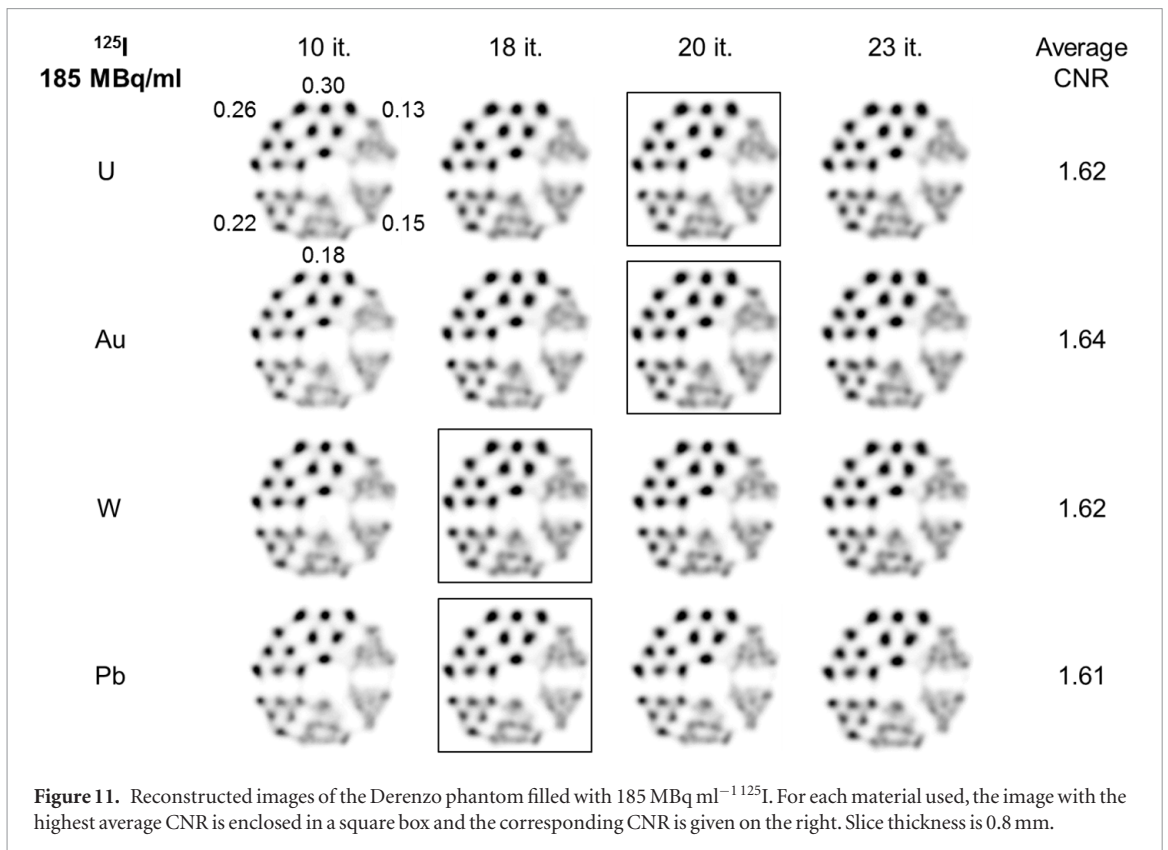
practical for EXIRAD-3D when long-lived isotopes are used because the tissue sample is cryo-cooled and its shape can be kept unchanged for a long scan.

The MCSs in this work are expected to well resemble realistic scans as they considered all important physics processes in SPECT (photoelectric effect, Compton scattering, and Rayleigh scattering for gamma photons, and ionisation, bremsstrahlung, and multiple scattering for electrons) as well as the realistic isotopes' energy distributions, background radiation, and detector response. In this work, MCS was used to mimic most of the imaging procedures, except the matrix interpolation. In principle, a full MCS could also be used to make the matrix by simulating point sources at every voxel, but for this high-resolution system that would take a prohibitively long computation time. Instead, a limited set of point spread functions was simulated, and the rest was obtained by



a well-validated interpolation method (van der Have *et al* 2008). This enabled accurate evaluation of pinhole material in micron-resolution SPECT in a reasonable time.

When choosing the pinhole material, besides the photon attenuation characteristics, the feasibility of using that material should be considered. Depleted uranium is hard to manufacture and not commonly available. In addition, it releases toxic oxide and background radiation. This background radiation can be minimised using small depleted uranium inserts by minimising the amount of uranium needed (Jaszczak 1999). We did not



include background radiation from the depleted uranium inserts in the simulation because the exact sizes of the inserts were not determined in this work. Gold is expensive, but gold or platinum-gold alloy can be produced at a reasonable expense for small pinhole inserts (Tenney *et al* 2001, Beekman *et al* 2002, Peterson *et al* 2002, van der Have *et al* 2009). Pure tungsten is hard to be cast owing to its high melting point, so tungsten alloys are usually used for easier machining at the cost of slightly decreasing its photon attenuation ability. For example, while pure tungsten has an attenuation coefficient of 0.952 mm^{-1} at 245 keV, the corresponding value for 92.5% W + 5.25% Ni + 2.25% Fe is 0.861 mm^{-1} (NIST). According to our simulations (see supplementary data (stacks.iop.org/PMB/64/105017/mmedia)), for ^{111}In imaging this results in only 2.9% reduction in the average SNR which meagrely affects the visual image quality. We expect that this difference is even smaller for lower energies or ‘purer’ tungsten alloys. Lead performs notably worse than the other studied materials (figures 8 and 9). Considering those aspects, gold and tungsten are preferred as materials for the pinhole collimator in EXIRAD-3D.

5. Conclusion

The influence of collimator material used in the micron-resolution SPECT system EXIRAD-3D has been studied by comparing resolutions that can be obtained when different pinhole materials are used while keeping sensitivity constant. Results indicate that using materials with higher stopping power yields images with better CNR for the studied isotopes with improvements ranging from 1.9% to 36.6%. Visual assessment of the reconstructed images suggests that for the EXIRAD-3D, the tungsten collimator is generally a good choice for a wide range of SPECT isotopes. For relatively high-energy isotopes such as ^{111}In , using gold inserts can be beneficial.

Acknowledgments

The authors would like to thank Ruud Ramakers and Sofia Koustoulidou (MILabs B.V.) for providing the data of the mouse knee joint scan, and the background radiation measurements.

References

- Accorsi R and Metzler S D 2004 Analytic determination of the resolution-equivalent effective diameter of a pinhole collimator *IEEE Trans. Med. Imaging* **23** 750–63
- Anger H O 1958 Scintillation camera *Rev. Sci. Instrum.* **29** 27–33
- Beekman F and Van Der Have F 2007 The pinhole: gateway to ultra-high-resolution three-dimensional radionuclide imaging *Eur. J. Nucl. Med. Mol. Imaging* **34** 151–61
- Beekman F J, McElroy D P, Berger F, Gambhir S S, Hoffman E J and Cherry S R 2002 Towards *in vivo* nuclear microscopy: iodine-125 imaging in mice using micro-pinholes *Eur. J. Nucl. Med.* **29** 933–8
- Beekman F J, van der Have F, Goorden M C, Vaissier P E B, van Roosmalen J and During H 2015 G-SPECT-I: a full ring high sensitivity and ultra-fast clinical molecular imaging system with <3 mm resolution *Eur. J. Nucl. Med. Mol. Imaging* **42** S209
- Beekman F J, van der Have F, Vastenhouw B, van der Linden A J A, van Rijk P P, Burbach J P H and Smidt M P 2005 U-SPECT-I: a novel system for submillimeter-resolution tomography with radiolabeled molecules in mice *J. Nucl. Med.* **46** 1194–200
- Bocher M, Blevins I M, Tsukerman L, Shrem Y, Kovalski G and Volokh L 2010 A fast cardiac gamma camera with dynamic SPECT capabilities: design, system validation and future potential *Eur. J. Nucl. Med. Mol. Imaging* **37** 1887–902
- Bom V, Goorden M and Beekman F 2011 Comparison of pinhole collimator materials based on sensitivity equivalence *Phys. Med. Biol.* **56** 3199–214
- Bowen J D, Huang Q, Ellin J R, Lee T-C, Shrestha U, Gullberg G T and Seo Y 2013 Design and performance evaluation of a 20-aperture multipinhole collimator for myocardial perfusion imaging applications *Phys. Med. Biol.* **58** 7209–26
- Chen C L, Wang Y, Lee J J S and Tsui B M W 2008 Integration of SimSET photon history generator in GATE for efficient Monte Carlo simulations of pinhole SPECT *Med. Phys.* **35** 3278–84
- Chen L, Tsui B M W and Mok G S P 2017 Design and evaluation of two multi-pinhole collimators for brain SPECT *Ann. Nucl. Med.* **31** 1–13
- Chu S Y F, Ekstrom L P and Firestone R B 1998 *Table of Radioactive Isotopes* (Sweden: Lund University) (<http://nucleardata.nuclear.lu.se/toi/index.asp>)
- Copeland D E and Benjamin E W 1949 Pinhole camera for gamma-ray sources *Nucleonics* **5** 44–9
- Furenlid L R, Wilson D W, Chen Y C, Kim H, Pietraski P J, Crawford M J and Barrett H H 2004 FastSPECT II: a second-generation high-resolution dynamic SPECT imager *IEEE Trans. Nucl. Sci.* **51** 631–5
- Golestani R, Wu C, Tio R A, Zeebregts C J, Petrov A D, Beekman F J, Dierckx R A J O, Boersma H H and Slart R H J A 2010 Small-animal SPECT and SPECT/CT: application in cardiovascular research *Eur. J. Nucl. Med. Mol. Imaging* **37** 1766–77
- Goorden M C, van der Have F, Kreuger R, Ramakers R M, Vastenhouw B, Burbach J P H, Booi J, Molthoff C F M and Beekman F J 2013 VECTor: a preclinical imaging system for simultaneous submillimeter SPECT and PET *J. Nucl. Med.* **54** 306–12
- Hamamatsu 2007 *Photomultiplier Tubes: Basics and Applications* 3rd edn (Japan: Hamamatsu Photonics K. K.)
- Hargreaves R, Hoppin J, Sevigny J, Patel S, Chiao P, Klimas M and Verma A 2015 Optimizing central nervous system drug development using molecular imaging *Clin. Pharmacol. Ther.* **98** 47–60
- Hesterman J Y, Kupinski M A, Furenlid L R, Wilson D W and Barrett H H 2007 The multi-module, multi-resolution system (M3R): a novel small-animal SPECT system *Med. Phys.* **34** 987–93
- Hijnen N M, de Vries A, Blange R, Burdinski D and Gröll H 2011 Synthesis and *in vivo* evaluation of 201Tl(III)-DOTA complexes for applications in SPECT imaging *Nucl. Med. Biol.* **38** 585–92
- Hubbell J H and Seltzer S M 1995 Tables of x-ray mass attenuation coefficients and mass energy-absorption coefficients (Online: <http://physics.nist.gov/PhysRefData/XrayMassCoef/cover.html>)
- Ivashchenko O, van der Have F, Villena J L, Groen H C, Ramakers R M, Weinans H H and Beekman F J 2014 Quarter-millimeter-resolution molecular mouse imaging with U-SPECT+ *Mol. Imaging* **13**
- Jan S et al 2011 GATE V6: a major enhancement of the GATE simulation platform enabling modelling of CT and radiotherapy *Phys. Med. Biol.* **56** 881–901
- Jan S et al 2004 GATE: a simulation toolkit for PET and SPECT *Phys. Med. Biol.* **49** 4543–61
- Jaszczak R J 1999 Uranium pinhole collimators for I-131 SPECT imaging *IEEE Trans. Nucl. Sci.* **46** 1165–71
- Kim H, Furenlid L R, Crawford M J, Wilson D W, Barber H B, Peterson T E, Hunter W C J, Liu Z, Woolfenden J M and Barrett H H 2006 SemiSPECT: a small-animal single-photon emission computed tomography (SPECT) imager based on eight cadmium zinc telluride (CZT) detector arrays *Med. Phys.* **33** 465–74
- King M A, Mukherjee J M, Konik A, Zubal I G, Dey J and Licho R 2016 Design of a multi-pinhole collimator for I-123 DaTscan imaging on dual-headed SPECT systems in combination with a fan-beam collimator *IEEE Trans. Nucl. Sci.* **63** 90–7
- Lee T-C, Ellin J R, Huang Q, Shrestha U, Gullberg G T and Seo Y 2014 Multipinhole collimator with 20 apertures for a brain SPECT application *Med. Phys.* **41** 112501
- Levenberg K 1944 A method for the solution of certain non-linear problems in least squares *Q. Appl. Math.* **2** 164–8

- Mallard J R and Myers M J 1963 The performance of a gamma camera for the visualization of radioactive isotope *in vivo* *Phys. Med. Biol.* **8** 165–82
- Maple C 2003 Geometric design and space planning using the marching squares and marching cube algorithms *Int. Conf. on Geometric Modeling and Graphics, 2003. Proc.* (IEEE Computer Society) pp 90–5
- Marquardt D W 1963 An algorithm for least-squares estimation of nonlinear parameters *J. Soc. Ind. Appl. Math.* **11** 431–41
- McDougal F and Tornai M 2017 Molecular breast imaging using a fully tomographic stationary clinical cardiac SPECT scanner: a phantom study *J. Nucl. Med.* **58** 1364
- Mejia J, Galvis-Alonso O Y, Castro A A de, Braga J, Leite J P and Simões M V 2010 A clinical gamma camera-based pinhole collimated system for high resolution small animal SPECT imaging *Braz. J. Med. Biol. Res.* **43** 1160–6
- Meng L J, Fu G, Roy E J, Suppe B and Chen C T 2009 An ultrahigh resolution SPECT system for I-125 mouse brain imaging studies *Nucl. Instrum. Methods Phys. Res. A* **600** 498–505
- Metzler S D and Accorsi R 2005 Resolution- versus sensitivity-effective diameter in pinhole collimation: experimental verification *Phys. Med. Biol.* **50** 5005–17
- Miwa K, Inubushi M, Takeuchi Y, Katafuchi T, Koizumi M, Saga T and Sasaki M 2015 Performance characteristics of a novel clustered multi-pinhole technology for simultaneous high-resolution SPECT/PET *Ann. Nucl. Med.* **29** 460–6
- Moszyński M, Zalipska J, Balcerzyk M, Kapusta M, Mengesha W and Valentine J D 2002 Intrinsic energy resolution of NaI(Tl) *Nucl. Instrum. Methods Phys. Res. A* **484** 259–69
- Nguyen M P, Ensing W, Vastenhouw B, Kamphuis C, Ramakers R, Goorden M C and Beekman F J 2017 System modeling and image reconstruction for 3D micron-resolution autoradiography NSS-MIC (https://www.eventclass.org/contxt_ieee2017/online-program/session?s=M-08#3193)
- NIST 2019 Element/compound/mixture (<https://physics.nist.gov/PhysRefData/Xcom/html/xcom1.html>)
- Nuyts J, Vunckx K, Defrise M and Vanhove C 2009 Small animal imaging with multi-pinhole SPECT *Methods* **48** 83–91
- Ogawa K, Harata Y, Ichihara T, Kubo A and Hashimoto S 1991 A practical method for position-dependent Compton-scatter correction in single photon emission CT *IEEE Trans. Med. Imaging* **10** 408–12
- Peterson M, Strand S-E and Ljungberg M 2015 Using the alloy Rose's metal as pinhole collimator material in preclinical small animal imaging: a Monte Carlo evaluation *Med. Phys.* **42** 1698–709
- Peterson T F, Hyunki K, Crawford M J, Gershman B M, Hunter W C J, Barber H B, Furenlid L R, Wilson D W, Woolfenden J M and Barrett H H 2002 SemiSPECT: a small-animal imaging system based on eight CdZnTe pixel detectors *2002 IEEE Nuclear Science Symp. Conf. Record vol 3* (IEEE) pp 1844–7
- Rong X, Du Y, Ljungberg M, Rault E, Vandenbergh S and Frey E C 2012 Development and evaluation of an improved quantitative 90Y bremsstrahlung SPECT method *Med. Phys.* **39** 2346
- Saint-Gobain 2019 NaI(Tl) and Polyscin® NaI(Tl) sodium iodide scintillation material (<https://www.crystals.saint-gobain.com/products/nai-sodium-iodide>)
- Sánchez F et al 2013 ALBIRA: a small animal PET/SPECT/CT imaging system *Med. Phys.* **40** 051906
- Schramm N, Hoppin J, Lackas C, Forrer F, Valkema R and de Jong M 2006 The NanoSPECT: a high-sensitivity multi-pinhole SPECT system with submillimeter (nanoliter) spatial resolution for imaging small rodents *J. Nucl. Med.* **47** 233P
- Seltzer S M 1993 Calculation of photon mass energy-transfer and mass energy-absorption coefficients *Radiat. Res.* **136** 147
- Staelens S, Vunckx K, Beenhouwer J De, Beekman F, Asseler Y D, Nuyts J and Lemahieu I 2006 GATE simulations for optimization of pinhole imaging *Nucl. Instrum. Methods Phys. Res. A* **569** 359–63
- Tenney C R, Tornai M P, Smith M F, Turkington T G and Jaszczak R J 2001 Uranium pinhole collimators for 511 keV photon SPECT imaging of small volumes *IEEE Trans. Nucl. Sci.* **48** 1483–9
- Tornai M P, Bowsher J E, Jaszczak R J, Pieper B C, Greer K L, Hardenbergh P H and Coleman R E 2003 Mammothography with pinhole incomplete circular orbit SPECT *J. Nucl. Med.* **44** 583–93
- Vaissier P E B, Beekman F J and Goorden M C 2016 Similarity-regulation of OS-EM for accelerated SPECT reconstruction *Phys. Med. Biol.* **61** 4300–15
- van der Have F and Beekman F J 2004 Photon penetration and scatter in micro-pinhole imaging: a Monte Carlo investigation *Phys. Med. Biol.* **49** 1369–86
- van der Have F, Vastenhouw B, Ramakers R M, Branderhorst W, Krah J O, Ji C, Staelens S G and Beekman F J 2009 U-SPECT-II: an ultra-high-resolution device for molecular small-animal imaging *J. Nucl. Med.* **50** 599–605
- van der Have F, Vastenhouw B, Rentmeester M and Beekman F J 2008 System calibration and statistical image reconstruction for ultra-high resolution stationary pinhole SPECT *IEEE Trans. Med. Imaging* **27** 960–71
- van Roosmalen J, Goorden M C and Beekman F J 2016 Molecular breast tomosynthesis with scanning focus multi-pinhole cameras *Phys. Med. Biol.* **61** 5508
- Vastenhouw B and Beekman F 2007 Submillimeter total-body murine imaging with U-SPECT-IJ. *Nucl. Med.* **48** 487–93
- Walker M D, Goorden M C, Dinelle K, Ramakers R M, Blinder S, Shirmohammad M, van der Have F, Beekman F J and Sossi V 2014 Performance assessment of a preclinical PET scanner with pinhole collimation by comparison to a coincidence-based small-animal PET scanner *J. Nucl. Med.* **55** 1368–74
- Willekens S M A, Joosten L, Boerman O C, Balhuizen A, Eizirik D L, Gotthardt M and Brom M 2016 Strain differences determine the suitability of animal models for noninvasive *in vivo* beta cell mass determination with radiolabeled exendin *Mol. Imaging Biol.* **18** 705–14